

Planetary Delay-Doppler Radar and the Long-Code Method

John K. Harmon

Abstract—Delay-Doppler mapping continues to be the most widely used imaging technique in radar astronomy. Various methods have been devised to partition echoes in delay-Doppler space for different degrees of echo dispersion (as quantified by the overspreading factor F). These include the standard interpulse/intercode methods for underspread ($F < 1$) or slightly overspread ($F > 1$) echoes, intrapulse methods for grossly overspread echoes, and the long-code method for the intermediate case of moderate overspreading. Here the standard and long-code methods are compared, treating various aspects of experiment design, data analysis, and calibration. Recent and future applications of the long-code method are also reviewed.

Index Terms—Coding, delay-Doppler mapping, planetary radar, pulse compression, radar.

I. INTRODUCTION

DELAY-DOPPLER mapping is an essential tool of radar astronomy. Forty years after its first successful demonstration [1], delay-Doppler mapping is still the most widely used imaging technique in the field. (Its only serious rival has been synthesis imaging with the Goldstone/Very Large Array (VLA) system [2], [3].) The continued utility and success of delay-Doppler imaging owes much to improvements in radar telescopes and systems, as well as to new developments in waveform selection and mapping.

The power of delay-Doppler mapping derives from its ability to image an echo at a resolution much finer than is possible with the real-aperture beam of the antenna. It does this by a two-step process.

- Step 1) Partitioning the echo from a deep, fluctuating target into cells in delay-Doppler space.
- Step 2) Mapping from delay-Doppler space into the target's natural (real-space) coordinates.

The basic method bears some similarity to synthetic aperture radar (SAR) and, in particular, to those techniques often referred to as “inverse SAR” (ISAR) and “spotlight SAR” [4]–[6]. In its practical implementation, however, planetary delay-Doppler imaging is usually much simpler than SAR imaging, as it normally ignores such effects as range walk and range curvature (an exception being the SAR-like mapping of the moon by Stacy [7]).

Despite this relative simplicity, planetary delay-Doppler imaging is beset by certain fundamental problems, the solutions

to which are by no means trivial. The toughest challenge confronting echo partitioning is the avoidance of delay folding and Doppler aliasing of the highly dispersed echoes from “overspread” targets. (This is related to the familiar “ambiguity” problem encountered in SAR imaging.) The mapping step from delay-Doppler to real space can also be problematic. Although relatively insensitive to the SAR “layover” effect, planetary mapping is subject to a more serious global mapping ambiguity about the Doppler equator, often called the “north–south ambiguity.” Apart from this, delay-Doppler reflectivity mapping of large, nearly spherical planets is a simple mathematical problem [8]. This is certainly not the case for small, irregular targets such as near-earth asteroids, for which the determination of shape and spin-state has to be part of the mapping solution. The mapping of such objects is a daunting task and one that is resistant to systematic algorithms, although some success has been achieved using least squares inversion methods [9].

Although the mapping problem is interesting *per se*, this paper is concerned only with echo partitioning. The purpose here is to discuss the current state of the delay-Doppler partitioning problem and to present a more thorough treatment of the long-code method, which was developed for delay-Doppler imaging of overspread targets such as Mars [10], [11]. We begin with a brief survey of the different methods used to measure the delay-Doppler array, so as to place the long-code method in its appropriate context. This is followed by a detailed comparison of the standard and long-code methods, addressing technical issues such as data acquisition and analysis, filtering, noise and clutter optimization, and calibration. The paper concludes with a discussion of some recent and future applications of the long-code method.

II. SURVEY OF DELAY-DOPPLER METHODS

The first objective in designing a delay-Doppler experiment is to partition the target echo (or some suitable portion of it) into delay-Doppler cells with a minimum of distortion. Different methods have been devised over the years to do this. The most important factor dictating the choice of method is the degree of dispersion of the echo, as quantified by the overspreading factor $F = TB$ (where T is the target's delay depth, and B is its Doppler bandwidth). Targets are said to be either “underspread” if $F < 1$ or “overspread” if $F > 1$. For a spherical planet of radius r and apparent rotation period t_r , one has $T = 2r/c$ and $B = 8\pi r\nu |\sin \alpha|/ct_r$, giving

$$\begin{aligned} F &= 16\pi r^2 \nu |\sin \alpha|/c^2 t_r \\ &= 6.47 \times 10^{-6} r^2 (\text{km}) \nu (\text{GHz}) |\sin \alpha|/t_r (\text{days}) \end{aligned} \quad (1)$$

Manuscript received August 2, 2001; revised July 8, 2002. Portions of this work were presented in the radar techniques sessions at the 2000 Progress in Electromagnetics Research Symposium in Cambridge, MA, and the 2001 National Radio Science Meeting in Boulder, CO.

The author is with the Arecibo Observatory, National Astronomy and Ionosphere Center, Arecibo, Puerto Rico 00612 (e-mail: harmon@naic.edu).

Digital Object Identifier 10.1109/TGRS.2002.803731

TABLE I
ECHO DISPERSION FACTOR F AT $\nu = 2.4$ GHz

Target	F
Mercury	1.1–1.7
Venus	1.3–4.2
Moon	0.7
Mars	170
Ceres	9
Pallas	4
Kleopatra	0.5
Toutatis	10^{-5}
Castalia	10^{-4}
Io	29
Europa	11
Ganymede	15
Callisto	5
Titan	6
Saturn Rings	10^6

where ν is the radar frequency; c is the speed of light; and α is the angle between the apparent rotation axis and the line of sight. Solar system targets span a wide range of F , which explains why no single delay-Doppler method handles all applications. Table I lists F values at S band ($\nu = 2.4$ GHz). Table II shows a breakdown of the various methods by F -range and radar type. This is intended as a rough guide only; in practice, and historically, the method boundaries are blurred, as is discussed below. The field of ionospheric incoherent scatter radar (ISR) faces echo dispersion problems similar to those encountered in radar astronomy, for which it has developed a suite of methods similar to those in Table II; the long-code method was, in fact, borrowed directly from ISR. For a discussion of delay-Doppler methods in ISR, see [12] and [13]. For a survey of planetary delay-Doppler methods before the advent of long-code, see [14].

A. Standard (Interpulse/Intercode) Method

Interpulse and intercode delay-Doppler (Table II), which we will refer to collectively as the “standard method,” was the first delay-Doppler method to be developed and is still the most commonly used. One transmits either a coherent train of identical pulses, if using a pulsed radar, or a coherent sequence of repeated codes, if using a continuous wave (CW) radar. (In pulsed radar, one can also code within the pulse, although this is rarely done in planetary radar.) At any given delay, samples from successive pulse repetition cycles (or decoded code cycles) are then summed coherently with various phase rotations (i.e., Fourier transformed) and squared to produce a Doppler spectrum for that delay. The collection of these spectra for the various delay bins comprises a two-dimensional array of echo power in delay-Doppler space. The sampling interval for the spectral analysis is the pulse or code repetition period p , which gives a spectral bandwidth of $1/p$. Hence, the full delay-Doppler echo can be recovered without delay folding ($p > T$) and Doppler aliasing ($1/p > B$) only if the echo is underspread ($TB = F < 1$).

The standard technique was conceived by Green [15] and first tested by Pettengill [1] in moon observations with the ultrahigh-frequency (440-MHz) pulsed radar at Millstone Hill.

TABLE II
DELAY-DOPPLER METHODS BY F -REGIME AND RADAR TYPE (PULSED, CW)

F	Pulsed	CW
< 1 (underspread)	interpulse (coherent pulse train)	intercode (coherent code sequence)
> 1 (overspread)	coded long pulse	long code
$>> 1$	intrapulse (long pulse)	frequency step

Delay-Doppler imaging of the moon was continued over the next decade at Haystack and Arecibo. Standard delay-Doppler has also been used with great success to image Venus, beginning with Goldstone observations [16] and culminating in the high-resolution imaging with the Arecibo S band radar [17]. Standard delay-Doppler has been used to image Mercury’s equatorial regions [18], [19] and putative polar ice deposits [20]. Standard delay-Doppler cannot be used to image the highly overspread Mars, although template fitting to the leading edge of the delay-Doppler echo has been used to measure Martian topography and quasi-specular scattering parameters along the Doppler equator [21]–[23]; the same technique has been used to measure equatorial topography on Mercury [18], [19], [24], [25]. The past decade has also seen some successes in radar imaging of near-earth asteroids with standard delay-Doppler [26]–[28].

B. Intrapulse Methods

Intrapulse (or long-pulse) methods offer an alternative delay-Doppler approach for highly overspread objects. Here, as in standard pulsed delay-Doppler, one uses a pulse train with an interpulse period longer than the target delay depth ($p > T$) to avoid delay folding of the echo. The difference is that one then does the coherent analysis only within the pulse, the Doppler spectra from successive pulse cycles being summed incoherently (for each delay). An analogous method has been developed for CW radar that uses cyclic stepping of the transmitter frequency to synthesize pulses. In this case, the frequency dwell time corresponds to the pulse width, and the cycle time of the frequency step sequence corresponds to the interpulse period p . Frequency aliasing is avoided by making the frequency step larger than the target bandwidth B . Since the frequency resolution is $\Delta f = 1/\Delta t$, where Δt is the pulse width, the maximum number of delay-Doppler cells into which one can resolve the overspread echo is $(B/\Delta f)(T/\Delta t) = TB = F$.

Intrapulse mapping of Mars has been done with the 430-MHz pulsed radar at Arecibo [29], albeit with very coarse resolution owing to the relatively small F at this frequency. Saturn’s rings, being much more highly overspread, are better suited to this method. Frequency-step delay-Doppler mapping of the rings was done with the S band CW radars at Arecibo and Goldstone in 1976 [30], and again very recently using the upgraded Arecibo S band radar [31].

C. Long-Code Method

Although the standard and intrapulse methods were suitable for many radar astronomy applications, there had always been a need for a way to deal with targets (notably Mars) in the intermediate F regime. An analogous situation existed in ionospheric ISR, where interpulse and intrapulse methods could be used on the lower and upper ionosphere, respectively, but were ill suited for intermediate altitudes [12]. The ISR techniques devised to fill this gap include the “coded long pulse” (CLP) method of Sulzer [12], [13] and the “alternating code” method of Lehtinen and Häggström [32]. In the CLP method, one transmits a long (nonrepeating) code. Then, instead of doing the standard cross-correlative decoding to obtain each sample of the time series for the spectral analysis, one does the spectral analysis directly on the lagged-product time series of the signal and code; in effect, the decoding and spectral analysis are done in the same operation. The code’s baud length b then defines both the delay resolution and the sampling interval for the spectral analysis, permitting one to recover an overspread delay-Doppler array without delay folding or Doppler aliasing. This comes, however, at the expense of some added clutter noise from the unwanted delays. It was realized that the CLP technique could be adapted for mapping overspread targets in radar astronomy. Hagfors and Kofman [33], [34] proposed a scheme based on the CLP principle and using Gaussian noise modulation. At the same time, Harmon and colleagues [10] developed a system for the Arecibo S band radar based on long pseudonoise phase codes. This CW-radar version of CLP has become known as the “long-code” method. The method was first tested at Arecibo during the 1990 Mars opposition [10], [11]. It has since been used for imaging Mercury [35]–[39], ranging and imaging the Galilean satellites [40], [41], and imaging the main-belt asteroids Kleopatra [42] and Ceres [43]. Since the baud must satisfy $1/b > B$ to avoid Doppler aliasing, one is constrained to have $T/b > F$ delay bins on the target, making this method unsuitable for grossly overspread targets such as Saturn’s rings (owing to the low detectability of such finely divided echoes).

III. STANDARD AND LONG-CODE METHODS: A COMPARISON

A. Radar Systems and Experiments

1) *Standard*: The schematic in Fig. 1 shows the basic elements of a radar system suitable for either standard or long-code delay-Doppler experiments. A typical experiment involves transmission of a modulated wave with circular polarization. In CW pulse compression, one normally uses a hardware device to generate a binary phase code according to a pseudonoise (PN) maximal-length shift-register sequence of length $L_c = p/b = 2^n - 1$ (integer n), where the phase flip interval (or “baud”) b equals the desired width of the compressed pulse. In standard intercode delay-Doppler, the code repetition period p is set long enough to avoid or minimize delay folding but short enough to avoid or minimize Doppler aliasing.

A typical delay-Doppler receiver is a two-channel system that receives both the “expected” or “polarized” sense circular (also called “OC” for “Opposite Circular”) and the “unexpected” or “depolarized” sense circular (or “SC” for “Same Circular”).

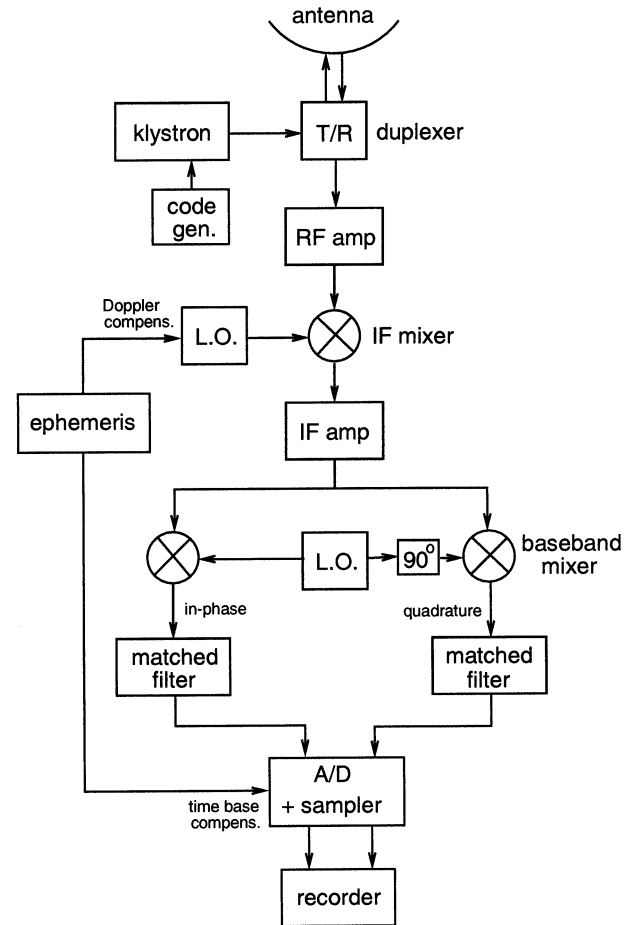


Fig. 1. Block diagram of a typical radar system suitable for either standard or long-code delay-Doppler observations.

The intermediate-frequency (IF) mixing is done with a programmable local oscillator whose frequency is continuously adjusted from a precomputed ephemeris to compensate for the target’s mean Doppler offset and drift; a similar compensation is also applied to the stretch and drift of the sampling time base. Detection is done with a quadrature baseband mixer, so Doppler spectra are two-sided with zero center frequency. The in-phase and quadrature outputs are passed through matched filters (matched to the baud), digitized, sampled (at least once per baud), and recorded for later analysis.

2) *Long-Code*: Although long-code experiments use the same basic system elements (Fig. 1) as the standard method, there are a few operational differences. One important difference is in the transmission coding. Whereas the standard method uses a repeating PN code, the long-code method uses a nonrepeating code to ensure randomness of the self-clutter. Hagfors and Kofman [33] proposed using phase and amplitude modulation with Gaussian noise. However, biphase coding is easier to implement on existing radars and less affected by “same-delay clutter” than is phase-amplitude modulation. Arecibo CLP observations of the ionosphere do the biphase modulation using a hardware-generated PN code whose repetition period p is set to be longer than the integration period to ensure randomness of the clutter statistics [12]. This same coding technique has been used for the Arecibo

long-code planetary radar observations. The only difference is that long-code observations with the S band CW radar employ a coded continuous transmission, whereas CLP observations with the 430-MHz pulsed radar use coded pulses; an implication is that the coherent integration time is limited to the pulse length for CLP, but can be as long as the echo round-trip time for long-code. Although code generation from random number generators is preferred over the shift-register method for long-code experiments, it is impractical, owing to limitations in real-time computer speed and memory. Fortunately, subsequences of long shift-register PN codes have been found to provide good approximations to random codes, as has been proven by simulation. The main drawback of shift-register coding employing feedback is that any system phase errors (as from transmitter ringing or unbalanced mixers) can introduce spurious correlations that show up as oscillations in the self-clutter spectrum at certain discrete delays in the transmission's ambiguity function. However, simulations show that this problem is peculiar to codes with two feedback taps and that the oscillations are virtually eliminated by using four-tap codes.

For most long-code applications, one can use the same matched-filtered receiver system and sampling rate (once per baud) as that used in standard delay-Doppler. An exception might be for long-code observations of highly overspread targets (e.g., Mars), where it may be preferable to run with a wider (unmatched) filter and denser (multisample/baud) sampling in order to reduce the filter-mismatch effect (Section III-C).

B. Decoding and Spectral Analysis

1) *Standard*: The analysis process used in standard inter-code delay-Doppler is illustrated in Fig. 2(a). The first step is decoding. Here one cross-correlates the data time series with the code, yielding a cross-correlation function (CCF) for each code cycle. The CCF calculation can be done efficiently using fast-correlation techniques based on the convolution theorem. (These employ long transforms over multiple code cycles, along with standard end-effect corrections [44].) At this point, the data are arranged as a stack of (complex) signal voltage-versus-delay profiles from successive code cycles. The coherent (spectral) analysis then consists of doing complex fast Fourier transforms (FFTs) across the stack, with one FFT for each delay. Taking the squared modulus then gives a real Doppler power spectrum for each delay. Since the sampling interval for the spectral analysis is the code cycle period p , each Doppler spectrum has a bandwidth of $1/p$ or a Nyquist frequency $f_N = 1/2p$. Also, the spectrum has a frequency resolution of $\Delta f = 1/L_t p$, where L_t is the FFT length in code cycles. Each delay-Doppler array estimate, or “look,” represents a single statistical realization of the echo (plus noise) power distribution in delay-Doppler space. One then beats down the statistical fluctuations by doing an incoherent summation of the delay-Doppler arrays from successive looks over some suitable integration time t_{int} . Examples of OC and SC delay-Doppler arrays from a standard-code observation of Mercury are shown in Fig. 3(a) and (b).

2) *Long-Code*: The differences between the long-code and standard intercode analyses are seen by comparing Fig. 2(a) and (b). In long-code there are no repeated code cycles, nor does

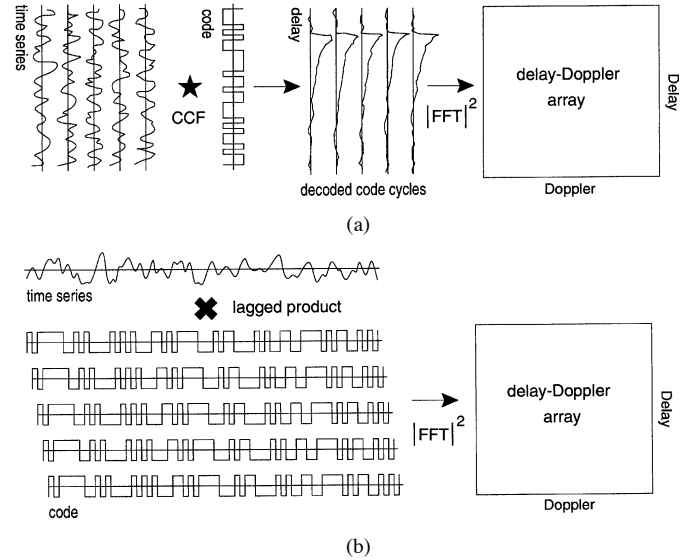


Fig. 2. Schematic illustrating the basic principles of delay-Doppler analysis for (a) the standard method and (b) the long-code method.

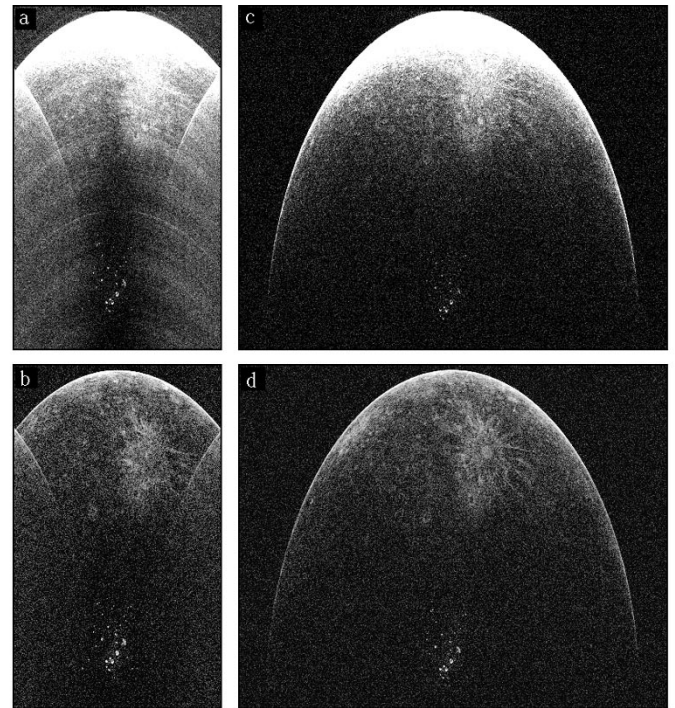


Fig. 3. Delay-Doppler arrays for Mercury obtained with the Arecibo S band radar. (a) Standard method, OC polarization. (b) Standard method, SC polarization. (c) Long-code method, OC polarization. (d) Long-code method, SC polarization. The vertical axis is delay (increasing toward the bottom), and the horizontal axis is Doppler. The delay axis extends 17 ms, and the Doppler axis extends (a), (b) 48.9 Hz or (c), (d) 101 Hz. The echo Doppler bandwidth B was either (a), (b) 85.1 Hz or (c), (d) 88.3 Hz. The standard-code observation was made on July 3, 1999 (sub-earth point at 7.6°N , 357.9°W). The long-code observation was made on June 16, 2000 (sub-earth point at 6.2°N , 358.2°W). The baud b was $20\ \mu$ in both cases. The echo's leading edge is at top; the polar “ice” spots are at bottom center; and the bright rayed crater called feature “A” is in between. The OC image grayscale is normalized to the polar features, so the leading edge specular echo is saturated.

one do a standard pulse-compression decode on any segment of the data time series (as this would impose a lowpass filtering on those high frequencies in the Doppler spectrum that

one wishes to recover). Instead, a lagged-product time series is formed for a given lag (or delay) by multiplying the sampled signal by the suitably lagged code, and then the power spectrum of this lagged-product time series is computed directly. (This is equivalent to multiplying the data time series by $e^{-i2\pi ft}$ and then cross correlating with the code, for each Doppler f .) One then builds the delay-Doppler array by performing this operation for the various lags, changing the lag in one-baud steps. The delay-Doppler arrays from successive looks are then summed incoherently to improve echo detectability. If sampling once per baud, then the Doppler spectra will have a bandwidth of $1/b$ ($f_N = 1/2b$), which can be set to be wider than the echo bandwidth to avoid Doppler aliasing. Also, since there are no repeated code cycles, there is no problem with delay folding of the echo. The frequency resolution of the delay-Doppler array is $\Delta f = 1/L_t b$, where L_t is the transform length. Examples of delay-Doppler arrays from a long-code observation are shown in Fig. 3(c) and (d). These were obtained at a sub-earth aspect close to that of the standard-code observation of Fig. 3(a) and (b). Note the lack of aliasing of the overspread Mercury echo in the long-code images, in contrast to the standard method.

The main drawback of long-code compared to standard delay-Doppler (i.e., the price paid for doing the decode and spectral analysis in the same operation) is that, for any given lag, the echo power from the other “wrong” (unsynchronized) delays is not subject to the strong filtering inherent in standard decoding. Instead, this power appears as a noise-like self-clutter (Section III-D) that, when added to the receiver noise, raises the overall background noise level.

Another drawback of the long-code method is the relatively slow data processing. In the standard method one does an efficient fast-correlation decode followed by an FFT (at each delay) on what amounts to a greatly decimated time series, whereas long-code must do an FFT on a lagged-product time series sampled at the baud rate. (One could convert this to a fast-correlation problem by doing inverse FFTs of lagged products in the transform domain, but this is more efficient only if one wants fewer Dopplers than delays.) Fortunately, for many overspread targets the echo bandwidth is still much less than the inverse of the baud ($B \ll 1/b$), in which case one can smooth and decimate the lagged-product time series before transforming, shortening the FFT length and substantially reducing computation time. (If n is the time-series length and one does an m -point smoothing and decimation, then the number of operations involved in processing each lag goes from $2n \log_2(n) + n$ down to $2(n/m) \log_2(n/m) + n$.) A simple boxcar smoothing is preferred, as it has the attractive property of maintaining the whiteness of the noise-plus-clutter background. As an example, the Mercury delay-Doppler arrays plotted in Fig. 3(c) and (d) were computed using a 256-point smoothing and decimation of the lagged-product time series. Continuing improvements in computer speed have also been a substantial help, making virtually all long-code data analysis problems practicable for desktop computers.

C. Signal, Noise, and Filtering

The end result of the foregoing standard or long-code echo processing is an estimated delay-Doppler array

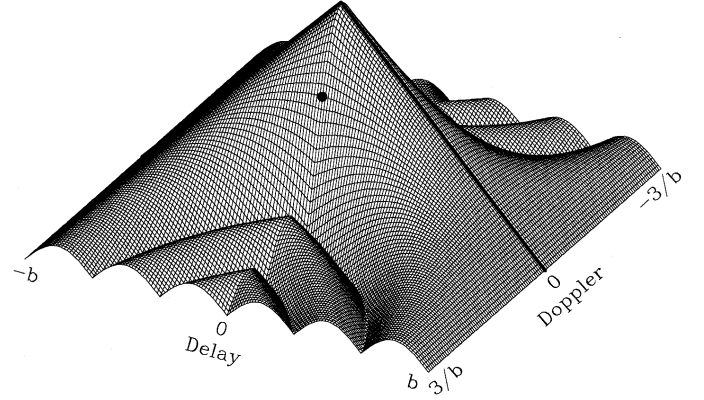


Fig. 4. Single-pulse ambiguity function modulus $|\chi(\tau, f)|$. The axis labels are in terms of the baud length b . Also shown are the triangle cut through $f = 0$ (heavy line) and the peak of the cut through the long-code Nyquist frequency $f_N = 1/2b$ (filled circle).

$A_{ij} \equiv A(\tau_i, f_j)$, where A_{ij} has units of power and where τ_i and f_j are the delay and frequency at the center of delay-Doppler cell i, j . This array can be written as

$$A_{ij} = S_{ij} + N_{ij} + C_{ij} \quad (2)$$

i.e., as the sum of contributions from echo signal S , system noise N , and self-clutter C . Signal and noise are discussed here, with clutter left to Section III-D. Here we will treat S , N , and C implicitly as expectation values of statistically fluctuating quantities. Later (Section III-E) we will consider the effect of noise and clutter fluctuations on echo detectability. Fluctuations in signal S , associated with “speckle” or “fading” noise, will not be considered here.

1) *Standard*: The echo power estimate S_{ij} can be expressed in terms of the true differential echo power distribution $S'(\tau, f)$, which is the power per unit delay and Doppler from a target surface element with delay τ and Doppler f . The differential contribution $S'_{ij}(\tau, f)$ to S_{ij} from a point echo at τ, f is given by (see Appendix I-A)

$$S'_{ij}(\tau, f) = H(L_c, bf) H(L_t, p[f - f_j]) \cdot \sum_k |\chi(\tau_i - \tau - kp, f)|^2 S'(\tau, f) \quad (3)$$

where

$$\chi(\tau, f) = \Lambda(\tau/b) \text{sinc}([b - |\tau|]f) e^{i\pi f \tau} \quad (4)$$

is the single-pulse ambiguity function (Fig. 4) and

$$H(L, x) = \left(\frac{\sin \pi L x}{L \sin \pi x} \right)^2. \quad (5)$$

Other symbols (in Bracewell’s [45] notation) are the triangle function $\Lambda(x) = 1 - |x|$ ($=0$ for $|x| > 1$) and $\text{sinc}(x) = \sin \pi x / \pi x$. The k -summation represents a delay ambiguity from the repeating code and accounts for any delay folding of the echo, while the $H(L_t, p[f - f_j])$ factor represents a Doppler ambiguity, accounting for any Doppler aliasing and defining the frequency resolution window. Assuming there is no delay folding (fix $k = 0$) or Doppler aliasing, and given

that $f \ll 1/b$, then the H functions approximate to sinc^2 functions, and we have

$$S'_{ij}(\tau, f) = K_{ij}(\tau, f) S'(\tau, f) \quad (6)$$

where

$$K_{ij}(\tau, f) = \text{sinc}^2(pf) \text{sinc}^2([f - f_j]/\Delta f) |\chi(\tau_i - \tau, f)|^2 \quad (7)$$

and $\Delta f = 1/L_t p$ is the frequency resolution. Then, integrating over τ, f (assuming incoherence of adjacent regions on the planet) gives

$$S_{ij} = \iint S'_{ij}(\tau, f) d\tau df = \iint K_{ij}(\tau, f) S'(\tau, f) d\tau df \quad (8)$$

which, given the narrowness of the $\text{sinc}^2(f/\Delta f)$ function, can be approximated by

$$S_{ij} \approx Y_j Z_j S'_{ij} b \Delta f \quad (9)$$

where S'_{ij} is the weighted average

$$S'_{ij} = \frac{\iint K_{ij}(\tau, f) S'(\tau, f) d\tau df}{\iint K_{ij}(\tau, f) d\tau df}. \quad (10)$$

Equation (9) conveniently expresses S_{ij} as a filtered version of $S'_{ij} b \Delta f$, which is the equivalent echo power from a rectangular cell measuring $b \times \Delta f$. The filter factors are a “code filter” $Y_j \equiv Y(f_j)$ and a “baud filter” $Z_j \equiv Z(f_j)$, where

$$Y(f) = \text{sinc}^2(pf) \quad (11)$$

and

$$Z(f) = \frac{1}{b} \int |\chi(\tau, f)|^2 d\tau = \frac{1}{b} \int \Lambda^2(\tau/b) e^{-i2\pi f\tau} d\tau. \quad (12)$$

The code filter Y expresses the lowpass filtering inherent in the decoding process, while the baud filter Z accounts for signal reduction by the delay and Doppler mismatches between an echo element and our matched-filter processor. The convenient Fourier transform identity for Z in (12) is derived in Appendix II. In most standard delay-Doppler, one has $f \ll 1/b$; so the Doppler mismatch is negligible, and the baud filter can be approximated by the constant factor

$$Z = \frac{1}{b} \int \Lambda^2(\tau/b) d\tau = \frac{2}{3}. \quad (13)$$

This represents the delay mismatch averaged over the resolution cell. It is important to include this factor when calibrating for radar cross section (see Section III-F).

The background noise power is a flat pedestal in delay-Doppler space with a mean level of

$$N = N_o \Delta f \quad (14)$$

where N_o is the noise spectral density (noise power per unit frequency). Hence, one can estimate S by simply subtracting a flat noise baseline, although care must be taken when the self-clutter C is significant (Section III-D). Another property of the noise component N is that its statistical fluctuations are uncorrelated between adjacent delay bins; this is important to note when

doing delay smoothing of an overresolved delay-Doppler array (Section III-E). Finally, dividing (9) by (14) gives a signal-to-noise ratio

$$(S/N)_{ij} \equiv \frac{S_{ij}}{N} = Y_j Z_j \left(\frac{S'_{ij} b}{N_o} \right). \quad (15)$$

2) *Long-Code*: The long-code equivalent of (3) is (see Appendix I-B)

$$S'_{ij}(\tau, f) = H(L_t, b[f - f_j]) |\chi(\tau_i - \tau, f)|^2 S'(\tau, f). \quad (16)$$

Note that there is no code-cycle ambiguity as in the standard case. This is a very useful property, as it not only ensures there will be no echo folding in delay, but also enables one to avoid the modulo- p code cycle ambiguity in obtaining absolute ranges to targets with uncertain delay ephemerides. (In standard delay-Doppler, this range ambiguity is usually resolved by measuring the change in echo offset within the delay window when the baud is changed slightly.) Assuming there is no Doppler aliasing, then the H function approximates to a sinc^2 function, and we have

$$S_{ij} \approx Z_j S'_{ij} b \Delta f. \quad (17)$$

From (17), we also see that there is no code filter Y ; this accounts for the strength of the high-Doppler wings in Fig. 3(c) and (d) when compared with the weaker, aliased wings in Fig. 3(a) and (b). Another difference with the standard case is that the baud filter Z can have a nonnegligible effect for highly overspread echoes with Doppler bandwidths approaching $1/b$. This filter-mismatch effect (associated with the mismatch between the baseband matched filter and the Doppler-offset echo) attenuates echo power at higher Dopplers, as can be calculated from the Fourier transform in (12). It also flattens the peak of the ambiguity function somewhat, although $|\chi|$ is well behaved in that it is still unimodal at the $1/2b$ Nyquist frequency and remains $2b$ wide at the base (see Fig. 4). If the filter-mismatch effect of Z is considered too strong, it can be reduced by shortening the baud or by running in unmatched mode. (The latter can be done by using an n -times-wider filter and then sampling and decoding with n samples per baud.) Finally, note that there will be an additional $\text{sinc}^2(mbf)$ filter if one does an m -point boxcar smoothing and decimation of the lagged-product time series as discussed in Section III-B.

For the usual case of once-per-baud sampling and decoding, the noise component has the same flat pedestal form with $N = N_o \Delta f$ as for the standard method. The corresponding S/N is

$$(S/N)_{ij} = Z_j \left(\frac{S'_{ij} b}{N_o} \right). \quad (18)$$

As in the standard case, the noise statistics are uncorrelated between different delays.

D. Self-Clutter

Here we adopt Rihaczek's [46] term “self-clutter” to denote the stray power contribution from either echo leakage into pulse compression sidelobes (standard) or “wrong-delay” clutter (long-code).

1) *Standard*: The function given in (4) only represents the central spike of the ambiguity function of a PN code. At zero Doppler, $|\chi|^2$ takes a “thumbtack” form, with a Λ^2 central spike and a flat pedestal of height $1/L_c^2$ at all other delays. Were this thumbtack shape to hold at all frequencies, the self-clutter from convolution of the echo with the pedestal would only contribute a flat component to the delay-Doppler array. However, away from zero Doppler this simple thumbtack shape no longer holds, as the pedestal breaks up into messy sidelobes whose peak amplitude increases with Doppler [47], [48]. Echo leakage into these sidelobes can be a nuisance when doing delay-Doppler on echoes with high dynamic range, and also complicates noise baseline subtraction. The effect is clearly seen in Fig. 3(a), which shows visible streaking from leakage of the strong leading edge of Mercury’s OC specular echo into the other delays. Several techniques exist for suppressing such sidelobes or their effects. These include deconvolution of the corrupted delay-Doppler array using the ambiguity function [20], digital phase mixing of each Doppler down to baseband before decoding, use of weighted or tapered decoding filters [49], and code extension of the transmitted code for those cases in which a noncyclic code is being used [7].

2) *Long-Code*: The ideal long-code experiment uses a truly random code, i.e., one whose autocorrelation function is zero for lags of one baud or greater. This ensures that there is no deterministic clutter such as that giving rise to the standard-code leakage effects [compare Fig. 3(a) and (c)]. However, given the nature of long-code decoding, one must accept the fact that the full echo power from all the other (unsynchronized) delays will appear as a random, noise-like self-clutter at any given delay. (Hagfors and Kofman [33], [34] refer to this component as “self-noise” rather than “self-clutter”). For the usual one-sample/baud decoding, this clutter component has a white spectrum between the $f_N = \pm 1/2b$ Nyquist frequencies. This just adds a white-noiselike clutter on top of the white system noise. The clutter power level at delay k is given by

$$C_k \approx b \Delta f \left(\sum_{i \neq k} \sum_j S_{ij} + \sum_j u_j S_{kj} \right) \quad (19)$$

which is obtained by integrating the differential clutter of (49) (Appendix I-B) over delay-Doppler cells. The second term of (19) gives an approximate correction for same-delay clutter, where

$$u_j = \frac{2}{bZ_j} \int_{b/2}^b |\chi(\tau, f_j)|^2 d\tau \quad (20)$$

is the fractional overlap between the squared ambiguity functions of adjacent delay bins. Ignoring this small correction, we can define a general clutter-to-noise ratio

$$C/N = b \Delta f \sum_i \sum_j (S/N)_{ij}. \quad (21)$$

Since the clutter spectrum is white, noise subtraction remains a simple matter of estimating and subtracting a mean baseline level. (Baseline subtraction is more complicated if running in

unmatched/multisample mode, as the self-clutter spectrum in that case is not white.) Because of the small variation in clutter level among the different delays (from the different same-delay clutter contributions), it is best to do a separate baseline estimate and subtraction for each delay. Also, the fact that the clutter appears as additive noise means that its contribution must be corrected for in any noise-based calibration (Section III-F). Finally, note that whereas the system noise spectra from different delays are uncorrelated, the clutter spectra from adjacent delays are slightly correlated. The overlap between the squared ambiguity functions of adjacent delay bins represents that portion of clutter power that is completely correlated between the two bins. It follows that the correlation coefficient ρ for the clutter between adjacent delay bins is $\rho = u^2$, where u is given by (20). This correlation is small, with $\rho = 1/64$ at $f = 0$.

E. Detectability and Resolution

In radar astronomy, as in radio astronomy, one distinguishes between S/N , which is the ratio of signal and noise power levels, and detectability D , which is the ratio of the signal (echo) power to the root-mean-square statistical fluctuation of the noise about the mean noise level. It is D , rather than S/N , that determines the quality of a delay-Doppler measurement.

1) *Standard*: Since successive realizations of the delay-Doppler array are statistically independent, one has

$$\frac{\sqrt{\text{var } N}}{N} = \frac{1}{\sqrt{t_{\text{int}}/L_t p}} = \frac{1}{\sqrt{t_{\text{int}} \Delta f}} \quad (22)$$

where $t_{\text{int}}/L_t p$ is the number of incoherent summations (looks) over the integration time t_{int} . Then, the detectability D is given by the radiometer equation

$$D_{ij} = \frac{S_{ij}}{\sqrt{\text{var } N}} = \sqrt{t_{\text{int}} \Delta f} (S/N)_{ij} \quad (23)$$

which gives $D \propto b\sqrt{\Delta f}$ from (15) if S'_{ij} is not changing with b (i.e., the echo structure is either resolved out or fairly dense and homogeneous). This shows the basic tradeoff between detectability and resolution. The frequency resolution Δf can be easily adjusted in the off-line analysis to strike a reasonable compromise, either by adjusting L_t in the coherent analysis or by doing a high-resolution coherent analysis and then smoothing back in Doppler. One does not have the same after-the-fact flexibility in the delay dimension. Let us assume that there is some preferred baud b that gives a good compromise between detectability and resolution for our purposes. Then, it is easily shown (Appendix III) that if one observes with a shorter baud b/m and then does an m -point delay smoothing of the delay-Doppler array, the detectability is \sqrt{m} worse than if one had used the longer baud b to begin with. In other words, in standard delay-Doppler one always pays a penalty for “overresolution,” i.e., for using a baud that is shorter than the delay resolution to which one ultimately smooths.

2) *Long-Code*: For the long-code case with self-clutter included, the detectability is given by

$$D_{ij} = \frac{S_{ij}}{\sqrt{\text{var } N + \text{var } C}} = \frac{\sqrt{t_{\text{int}} \Delta f} (S/N)_{ij}}{\sqrt{1 + (C/N)^2}}. \quad (24)$$

TABLE III

CLUTTER-TO-NOISE RATIOS FOR SELECTED TARGETS. VALUES ARE CALCULATED FOR THE UPGRADED ARECIBO S-BAND RADAR ASSUMING MINIMUM TARGET RANGE (INFERIOR CONJUNCTION OR OPPOSITION) AND USING THE TABULATED BAUD (SEE TEXT). THE ENTRY FOR IAA REPRESENTS THE GRAIN-COMA ECHO FOR COMET IRAS-ARAKI-ALCOCK

Target	Baud b (μ s)	$(C/N)_{OC}$	$(C/N)_{SC}$
Mercury	10	0.56	0.047
Venus	10	150	10
Mars	10	5.1	1.4
Ceres	100	0.002	0.0002
Kleopatra	100	0.004	0.0002
IAA (coma)	100	0.61	0.009
Io	250	0.011	0.002
Europa	250	0.045	0.069
Ganymede	250	0.071	0.102
Callisto	250	0.033	0.038

The clutter not only reduces the detectability, but also can alter the baud selection strategy. It is easily shown (Appendix III) that once clutter begins to dominate the noise ($C/N > 1$), it pays to deliberately overresolve and then smooth back in delay. This is because overresolution spreads the clutter power over a larger bandwidth and thus lowers the clutter spectral density relative to the noise spectral density (which remains the same). In fact, when clutter starts to dominate, the optimal strategy is to overresolve until the clutter and noise levels are equalized ($C/N = 1$), as was pointed out in [34]. However, even with optimal overresolution, the detectability is still a factor of $\sqrt{2C/N}$ worse because of the clutter (Appendix III). Also, since the OC and SC radar cross sections (and C/N ratios) can be quite different (Table III), one cannot optimally overresolve in both polarizations simultaneously.

F. Calibration (Radar Cross Section)

1) *Standard*: Radar calibration is normally done by comparing the echo power S with the noise baseline level N . One can estimate N by fitting a flat baseline to the Doppler spectra from the echo-free delays. This is then subtracted from the delay-Doppler array to give an estimate of S_{ij} . From (15) we have

$$\begin{aligned} S'_{ij} &= b^{-1} N_o Y_j^{-1} Z_j^{-1} (S/N)_{ij} \\ &\approx (3/2) b^{-1} k T_s Y_j^{-1} (S/N)_{ij}. \end{aligned} \quad (25)$$

Here we have used $Z = 2/3$ from (13) and $N_o = k T_s$, where T_s is system temperature and k is Boltzmann's constant. Then, using the radar equation and (25), $S'_{ij} b \Delta f$ can be normalized to a radar cross section array

$$\sigma_{ij} = g^{-1} S'_{ij} b \Delta f = (3/2) g^{-1} k T_s \Delta f Y_j^{-1} (S/N)_{ij}. \quad (26)$$

Here g is a radar-equation factor

$$g = \frac{P_t G^2 \lambda^2}{(4\pi)^3 R^4} \quad (27)$$

where P_t is transmitter power; G is antenna gain; λ is radar wavelength; and R is target distance.

For calibration purposes, (26) can be treated as the radar cross-section contribution from a rectangular resolution cell measuring $b \times \Delta f$. This implies that one can get the target's total cross section σ from

$$\sigma = \sum_i \sum_j \sigma_{ij}. \quad (28)$$

Likewise, one can synthesize a normalized version of the total target Doppler spectrum from

$$\sigma_j = \sum_i \sigma_{ij}. \quad (29)$$

This synthetic full-target Doppler spectrum can be useful for doing simplified scattering-law fits, although its S/N is significantly less than that of a spectrum from a Doppler-only (unmodulated transmission) observation. (Note that in the event of Doppler aliasing, the σ estimate from (28) will be biased low, since the correction for the code filter Y will be underestimated for the aliased frequencies.)

2) *Long-Code*: Clutter makes long-code calibration somewhat different from standard calibration. If one calibrates against system noise, then care must be taken to distinguish true system noise from clutter noise. There are two ways to do this, as discussed in [11].

- 1) Measure the true (clutter-free) system noise level by pointing off-source or by recording echo-free noise after the last transmission has been received.
- 2) Estimate the clutter level by taking the total (baseline subtracted) echo signal power and spreading it evenly over the full $1/b$ Nyquist bandwidth, then subtract this clutter level from the total (system + clutter) noise level (at echo-free delays) to get the system noise level N .

With N determined, one has

$$S'_{ij} = b^{-1} N_o Z_j^{-1} (S/N)_{ij} = b^{-1} k T_s Z_j^{-1} (S/N)_{ij} \quad (30)$$

so the radar cross-sectional array σ_{ij} is computed from

$$\sigma_{ij} = g^{-1} k T_s \Delta f Z_j^{-1} (S/N)_{ij} \quad (31)$$

where one can either compute Z from (12) or use $Z = 2/3$ (if $B \ll 1/b$). This σ_{ij} array can be used to compute a total cross section from (28) and a total Doppler spectrum from (29).

One can calibrate the clutter-to-noise ratio in a similar fashion using (21), (28), and (31). This gives (in the $B \ll 1/b$ approximation)

$$C/N = (2/3) g \sigma b / k T_s \quad (32)$$

which is just the ratio of the clutter spectral density $(2/3) g \sigma b$ to the noise spectral density $k T_s$, or the ratio of the total clutter power $(2/3) g \sigma$ to the total noise power $k T_s / b$. This can be useful for predicting and optimizing C/N for particular situations. Table III lists maximum C/N for various targets based on this equation. The bauds selected for Table III would give a reasonable compromise between resolution and S/N but are not necessarily optimized for C/N . Note also that since the OC and

SC cross sections will be different, one cannot optimize both polarizations simultaneously.

IV. LONG-CODE APPLICATIONS

A. Mars

Mars is a natural candidate for the long-code method, being highly (but not grossly) overspread and exhibiting strong spatial variations in radar reflectivity that show up well in full-disk radar images. The first long-code observations were made by Harmon and colleagues with the Arecibo S band radar during the 1990 Mars opposition, and these were followed up with additional observations during the 1992–1993 opposition [10], [11], [22]. Fig. 5(a) gives an example of an SC delay-Doppler array from December 1, 1990, showing the echo features associated with rough surfaces (mostly lava flows) in Elysium and Amazonis. The 1990–1993 observations were made using the canonical matched-filtered, one-sample/ baud setup with baud lengths of either 100 μ s (1990) or 70 μ s (1992–1993). Even with these rather long bauds, the Mars echoes suffered from low detectability, an unavoidable result of the low signal spectral density from the large Doppler spreading. Self-clutter also had a significant effect, with C/N for the SC echo ranging from 0.18–2.5 [2.0 for the echo in Fig. 5(a)].

The first opportunity to observe Mars with the upgraded Arecibo radar is the 2005 opposition. Planned observations will use shorter (~ 10 μ s) bauds in order to improve resolution, reduce clutter noise, and exploit the enhanced sensitivity of the new radar. However, clutter may still present a detectability problem for the OC polarization (Table III).

B. Mercury

Although the Mercury overspreading factor is small (Table I), the long-code method is useful for full-disk imaging, as it gives cleaner delay-Doppler images (Fig. 3) at the expense of negligible (for SC) to modest (for OC) noise increases from clutter (Table III). Long-code imaging results using the preupgrade Arecibo S band radar were reported in [35]–[37] based on 100- μ s-baud observations made in 1991–1992. Postupgrade long-code observations with 10–20- μ s bauds were made in the summers of 2000 and 2001 [38]. Fig. 3(c) and (d) shows the delay-Doppler arrays from one of the 2000 dates. Notable in these images are a prominent rayed crater (known as feature “A”) at intermediate delays and the putative north polar ice features at the tail of the echo. The polar features have also been imaged with the Goldstone X band (8.4 GHz) radar using the long-code method [39].

C. Outer Planet Satellites

The degree of overspreading of the Galilean satellites (Table I) makes them logical candidates for long-code radar. The first delay-Doppler detections of the Galilean satellites were the 100- μ s long-code observations of Ganymede and Callisto made at Arecibo in 1992 [40]. Given the weakness of the echoes with the preupgrade system, these observations were intended for ranging (for ephemeris refinement and orbital dynamics studies) rather than reflectivity mapping. The range estimates were obtained by cross-correlating the

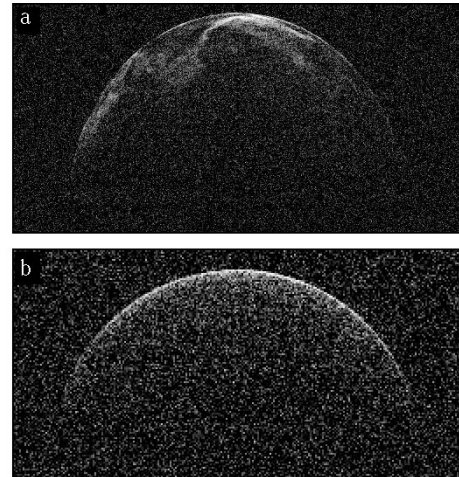


Fig. 5. Examples of delay-Doppler arrays from Arecibo long-code observations. (a) Mars and (b) Europa. The delay axis extends (a) 26 ms or (b) 13 ms, and the Doppler axis extends (a) 10 kHz or (b) 1.25 kHz. The echo Doppler bandwidth B was either (a) 7.835 kHz or (b) 1.014 kHz. The Mars image is a 6.7-min average from December 1, 1990 (sub-earth point at 9.7° S, 188.1° W). The Europa image is a 66-min average from November 7, 1999. The baud was 100 μ s in both cases.

entire delay-Doppler array with a model echo template. This optimized approach to long-code ranging [50] has potentially useful applications for other overspread outer planet satellites (e.g., Titan), even when the echoes are too weak for useful imaging. (Standard-code ranging of overspread targets using aliased templates can also be done, although the code-filter attenuation of the wings will reduce the quality somewhat.)

The recent Arecibo upgrade has yielded improvements in the quality of long-code delay-Doppler on the Galilean satellites and has even enabled some coarse reflectivity mapping (albeit with a north–south ambiguity). The new system was used to make the first delay-Doppler detections of Europa in 1999. An example of a Europa echo is shown in Fig. 5(b). This observation was made with a relatively short (100 μ s) baud for ranging purposes and at a time when the radar was only transmitting at half power. Observations in 2000 using longer (250–500 μ s) bauds and full power have since been made for reflectivity mapping of Europa, Ganymede, and Callisto [41].

D. Asteroids

Observations of near-earth asteroids (NEAs) and mainbelt asteroids (MBAs) make up an increasingly important component of the radar programs at Arecibo and Goldstone. Moreover, thanks to improved systems, an increasing fraction of asteroid work is being devoted to delay-Doppler observations. NEAs such as Toutatis and Castalia are small objects with $F \ll 1$ (Table I). Hence, standard delay-Doppler using short bauds is the method of choice for NEAs. Where the long-code method is more appropriate is in imaging the larger MBAs. Using 7 h as a typical rotation period for medium to large MBAs ($r > 100$ km) gives $F > 0.5$ for these objects, indicating that most are either overspread or close to it. Thus, the long-code method offers a safer and more flexible method for imaging and ranging MBAs in this size class. Recently, the Arecibo long-code system was used to image the medium-size MBA 216 Kleopatra [42].

Work has also commenced at Arecibo on long-code imaging of the largest MBAs (Ceres, Pallas, and Vesta), all of which are significantly overspread (Table I). Doing delay-Doppler mapping on these large MBAs remains difficult because of their weak echoes, although the Arecibo upgrade has brought at least crude imaging and optimized ranging within reach. The first delay-Doppler imaging of Ceres was done recently using the Arecibo long-code system [43], and more observations of this and other large MBAs are expected in the future.

E. Comets

Radar observations of a close-approaching comet can yield a narrow-band Doppler echo from the nucleus, a broad-band echo from a cloud of large (centimeter size) grains in the inner coma, or both [51]. All comet radar detections to date have been made in the Doppler-only mode, so obtaining a delay-Doppler detection of a comet (and, ultimately, high-resolution imaging of a nucleus) is one of the prime goals of radar astronomy. Since comet nuclei are highly underspread, standard delay-Doppler is preferred over long-code for nucleus imaging. On the other hand, long-code offers the best method for imaging the grain-coma echo. With their large Doppler bandwidths, the coma echoes for comets IRAS-Araki-Alcock ($B = 350$ Hz) and Hyakutake ($B = 3$ kHz) would have been overspread for grain cloud diameters in excess of 400 km and 50 km, respectively. Since the grain comae for these comets are thought likely to have been larger than these values (based on reasonable grain ejection velocities and lifetimes as well as shape modeling of the IRAS-Araki-Alcock echo), we conclude that these coma echoes must have been significantly overspread. For certain close-approaching comets then, the best strategy may be to do both standard and long-code observations.

V. SUMMARY AND CONCLUSION

Delay-Doppler radar comprises a suite of methods devised to handle various degrees of echo dispersion F . These methods include standard interpulse/intercode, long-pulse/frequency-step, and long-code, all of which are in current use. The standard method is the most efficient for underspread targets or when the overspreading is small enough to be ignored. Long-pulse methods are appropriate for any grossly overspread targets for which F delay-Doppler cells suffice and for which fewer than F delays are desired; in its CW frequency-step version, this method is still used to map Saturn's rings. The long-code method is finding increasing use for the intermediate case of moderate to large overspreading where more than F delay-Doppler cells are required and where placing more than F delays on the target is acceptable. The main reason for using long-code is, of course, to eliminate overspread aliasing. Secondary advantages include avoidance of deterministic self-clutter, range ambiguity, and code filtering (although, as pointed out earlier, techniques exist for dealing with delay sidelobes and range ambiguity in standard delay-Doppler). The main drawbacks of the long-code method are clutter noise, baud filtering, and slower data processing. Of these, clutter noise is the only fundamental problem, but one that can pose serious

limitations in some applications. Even with optimal overresolution, one suffers a factor of $\sqrt{2C/N}$ loss in detectability in clutter-dominated cases. Moreover, for highly specular targets like the terrestrial planets, the inability to optimize the clutter for both OC and SC polarizations simultaneously can present a serious problem. Recognizing this, Hagfors and Kofman [33] suggested a clever polarization-switching scheme to reduce long-code OC clutter by nulling out the strong specular glare at the echo's leading edge. Alternative methods should also be considered that are not based on the long-code principle at all and for which the self-clutter is inherently smaller. One possibility is coherent frequency stepping, a CW method that (as in the Saturn rings experiment) uses transmitter frequency stepping to synthesize pulses, but which maintains phase coherence between steps to enable interpulse spectral analysis. Such a method might be useful for future Mars mapping studies.

APPENDIX I

DELAY-DOPPLER PROCESSOR POINT-ECHO RESPONSE

Here it is assumed that the delay-Doppler processing is done on a data time series (time = t) that is complex-sampled once per baud b . We also assume that the spectral analysis is done in the customary fashion, i.e., using an unweighted (Bartlett) periodogram.

A. Standard

For our matched-filter delay-Doppler processor, the differential contribution to $S_{ij} + C_{ij}$ from a point echo of complex amplitude $a(\tau, f)$ is given by the periodogram

$$S'_{ij}(\tau, f) + C'_{ij}(\tau, f) = \left\langle \left| \frac{1}{L_t} \sum_{m=0}^{L_t-1} G(\tau_i - \tau + mp, f) a(\tau, f) e^{-i2\pi f_j mp} \right|^2 \right\rangle \quad (33)$$

where $\langle \rangle$ denotes expectation value, and G is the cross correlation

$$G(\tau, f) = c_1^*(t) \star \{ [c_2(t) \star \Pi(t/b)] e^{i2\pi ft} \star \Pi(t/b) \}. \quad (34)$$

Here $c_1(t)$ is a single cycle of the (δ -sequence) code of length L_c ; $c_2(t)$ is the repeating code; $\Pi(x)$ is the unit rectangle ($=1$ for $|x| < 1/2$, $=0$ for $|x| > 1/2$); and \star and $*$ denote correlation and convolution, respectively. (Note that $c_2 \star \Pi$ represents the transmitted waveform; $e^{i2\pi ft}$ is the echo Doppler carrier; and the second $\star \Pi$ convolution gives the action of the analog matched filter.) Using the associative property of convolution and the identity $[g(t) \star h(t)] e^{i2\pi ft} = [g(t) e^{i2\pi ft}] \star [h(t) e^{i2\pi ft}]$, we have

$$\begin{aligned} G(\tau, f) &= c_1^*(-t) \star \{ [c_2(t) \star \Pi(t/b)] e^{i2\pi ft} \star \Pi(t/b) \} \\ &= [c_1^*(-t) \star c_2(t) e^{i2\pi ft}] \star [\Pi(t/b) e^{i2\pi ft} \star \Pi(t/b)] \\ &= [c_1^*(t) \star c_2(t) e^{i2\pi ft}] \star \chi(\tau, f) \end{aligned} \quad (35)$$

where

$$\begin{aligned} \chi(\tau, f) &= \Pi(t/b) e^{i2\pi ft} \star \Pi(t/b) \\ &= \Lambda(\tau/b) \text{sinc}([b - |\tau|]f) e^{i\pi f\tau} \end{aligned} \quad (36)$$

is the single-pulse ambiguity function. Doing the correlation, we then have

$$G(\tau, f) = \left[\sum_n \delta(\tau - np) \frac{1}{L_c} \sum_{l=0}^{L_c-1} e^{i2\pi f(lb+\tau)} + \text{c.t.} \right] * \chi(\tau, f) \quad (37)$$

where c.t. represents a clutter term, and δ is the Dirac delta function. Ignoring clutter and a phase factor then gives

$$G(\tau, f) = \sqrt{H(L_c, bf)} \sum_n e^{i2\pi fnp} \chi(\tau - np, f) \quad (38)$$

where

$$H(L, x) = \left| \frac{1}{L} \sum_{l=0}^{L-1} e^{i2\pi lx} \right|^2 = \left(\frac{\sin \pi Lx}{L \sin \pi x} \right)^2 \quad (39)$$

is the familiar “grating” or Bartlett spectral window function. Putting (38) into (33) gives

$$S'_{ij}(\tau, f) = H(L_c, bf) \left\langle \left| \frac{1}{L_t} \sum_{m=0}^{L_t-1} \sum_n e^{i2\pi(fn-f_jm)p} \cdot \chi(\tau_i - \tau - np + mp, f) a(\tau, f) \right|^2 \right\rangle. \quad (40)$$

Changing the index variable to $k = n - m$ then gives

$$\begin{aligned} S'_{ij}(\tau, f) &= H(L_c, bf) \left\langle \left| \frac{1}{L_t} \sum_{m=0}^{L_t-1} e^{i2\pi(f-f_j)mp} \sum_k e^{i2\pi fkp} \cdot \chi(\tau_i - \tau - kp, f) a(\tau, f) \right|^2 \right\rangle \\ &= H(L_c, bf) H(L_t, p[f - f_j]) \\ &\quad \cdot \left\langle \left| \sum_k e^{i2\pi fkp} \chi(\tau_i - \tau - kp, f) a(\tau, f) \right|^2 \right\rangle. \end{aligned} \quad (41)$$

The k -summation in (41) represents the delay ambiguity from the repeating code. (This derivation ignores end effects on the $k \neq 0$ ambiguity contributions from the finite length of the transmission.) Using the fact that there is no overlap between k -surfaces (because of the narrowness of χ in delay), and defining $S'(\tau, f) = \langle |a(\tau, f)|^2 \rangle$, then

$$S'_{ij}(\tau, f) = H(L_c, bf) H(L_t, p[f - f_j]) \cdot \sum_k |\chi(\tau_i - \tau - kp, f)|^2 S'(\tau, f). \quad (42)$$

B. Long-Code

For the long-code processor, we have

$$\begin{aligned} S'_{ij}(\tau, f) + C'_{ij}(\tau, f) &= \left\langle \left| \frac{1}{L_t} \sum_{m=0}^{L_t-1} W(mb; \tau_i - \tau, f) a(\tau, f) e^{-i2\pi f_j mb} \right|^2 \right\rangle \end{aligned} \quad (43)$$

where W is the lagged-product time series

$$\begin{aligned} W(t; \tau, f) &= c^*(t) \left\{ [c(t + \tau) * \Pi(t/b)] e^{i2\pi f(t+\tau)} * \Pi(t/b) \right\} \\ &= c^*(t) \left\{ [c(t + \tau) e^{i2\pi f t}] * \chi(\tau, f) \right\} e^{i2\pi f \tau}. \end{aligned} \quad (44)$$

Writing the δ -sequence long-code $c(t)$ as $c_m = c(mb)$ and dropping the trailing phase factor in (44), we have

$$\begin{aligned} W(mb; \tau_i - \tau, f) &= c_m^* c_{m+n} e^{i2\pi f(m+n)b} \chi(r, f) \\ &\quad + c_m^* c_{m+n+l} e^{i2\pi f(m+n+l)b} \chi(r - lb, f) \end{aligned} \quad (45)$$

where n is the integer quotient of $(\tau_i - \tau)/b$; $r = \tau_i - \tau - nb$ is the remainder; and $l = \text{sgn}(\tau_i - \tau) = \pm 1$. For the case $n \neq 0$, both terms of (45) represent clutter terms. For $n = 0$, the second term is a clutter term, while the first term represents signal. Substituting this signal term into (43) gives

$$\begin{aligned} S'_{ij}(\tau, f) &= \left\langle \left| \frac{1}{L_t} \sum_{m=0}^{L_t-1} c_m^* c_m e^{i2\pi(f-f_j)mb} \chi(\tau_i - \tau, f) a(\tau, f) \right|^2 \right\rangle \\ &= H(L_t, b[f - f_j]) |\chi(\tau_i - \tau, f)|^2 S'(\tau, f). \end{aligned} \quad (46)$$

Putting the clutter terms of (45) into (43) gives

$$\begin{aligned} C'_{ij}(\tau, f) &= \left\langle \left| \frac{1}{L_t} \sum_{m=0}^{L_t-1} c_m^* c_{m+n} e^{i2\pi(f-f_j)mb} \right|^2 \right\rangle |\chi(r, f)|^2 \\ &\quad + \left\langle \left| \frac{1}{L_t} \sum_{m=0}^{L_t-1} c_m^* c_{m+n+l} e^{i2\pi(f-f_j)mb} \right|^2 \right\rangle \\ &\quad \cdot |\chi(r - lb, f)|^2 S'(\tau, f) \end{aligned} \quad (47)$$

for $n \neq 0$ and

$$\begin{aligned} C'_{ij}(\tau, f) &= \left\langle \left| \frac{1}{L_t} \sum_{m=0}^{L_t-1} c_m^* c_{m+l} e^{i2\pi(f-f_j)mb} \right|^2 \right\rangle \\ &\quad \cdot |\chi(\tau_i - \tau - lb, f)|^2 S'(\tau, f) \end{aligned} \quad (48)$$

for $n = 0$. Since the $\langle \rangle$ factors in (47) and (48) are all equal to $1/L_t = b \Delta f$, then

$$C'_{ij}(\tau, f) = \begin{cases} b \Delta f [|\chi(r, f)|^2 + |\chi(r - lb, f)|^2] S'(\tau, f), & n \neq 0 \\ b \Delta f |\chi(\tau_i - \tau - lb, f)|^2 S'(\tau, f), & n = 0. \end{cases} \quad (49)$$

APPENDIX II

BAUD FILTER IDENTITY

The identity in (12) gives a computationally convenient Fourier transform expression for the baud filter. One can prove this by starting from Parseval's theorem

$$Z(f) = \frac{1}{b} \int |\chi(\tau, f)|^2 d\tau = \frac{1}{b} \int |\mathcal{F}\{\chi(\tau, f)\}|^2 df' \quad (50)$$

where \mathcal{F} is the Fourier transform operator. Then, using the Fourier shift and convolution theorems, one has

$$\begin{aligned} Z(f) &= \frac{1}{b} \int |\mathcal{F}\{\Pi(t/b)\} \mathcal{F}\{\Pi(t/b) e^{i2\pi f t}\}|^2 df' \\ &= \frac{1}{b} \int |\text{sinc}(bf') \text{sinc}(b[f' - f])|^2 df' \\ &= \frac{1}{b} \text{sinc}^2(bf) * \text{sinc}^2(bf) = \frac{1}{b} \mathcal{F}\{\Lambda^2(\tau/b)\} \\ &= \frac{1}{b} \int \Lambda^2(\tau/b) e^{-i2\pi f \tau} d\tau. \end{aligned} \quad (51)$$

An alternative derivation in [46] gives the identity

$$\int |\chi(\tau, f)|^2 d\tau = \int |\chi(\tau, 0)|^2 e^{-i2\pi f \tau} d\tau \quad (52)$$

from which (51) follows directly.

APPENDIX III

OVERRESOLVED DETECTABILITY

We denote noise and clutter for the preferred baud b by N , C ; for the shorter observing baud b/m by N' , C' ; and for the final m -point delay-smoothed array by N'' , C'' . Then, for the standard method the overresolved noise variance is

$$\text{var } N'' = m \text{ var } N' = m \text{ var } N. \quad (53)$$

Then, since $S'' = S$, the overresolved detectability is given by

$$D'' = D \sqrt{\frac{\text{var } N}{\text{var } N''}} = \frac{D}{\sqrt{m}}. \quad (54)$$

For the long-code case, the variance of the final noise-plus-clutter background (ignoring the small interdelay clutter correlation ρ) is given by

$$\begin{aligned} \text{var } (N'' + C'') &= m \text{ var } N' + m \text{ var } C' \\ &= mN^2/n + C^2/mn. \end{aligned} \quad (55)$$

Here we have used the relations $\text{var } N' = \text{var } N = N^2/n$ and $\text{var } C' = \text{var}(C/m) = C^2/m^2n$, where n is the number of looks. Setting the derivative of (55) with respect to m equal to zero gives $m = C/N$ as the optimal overresolution factor to minimize the variance. One then has $C'/N' = (C/N)/m = 1$, which says that one optimizes by overresolving until clutter and noise are equalized. Putting $m = C/N$ into (55) and dividing by $\text{var } N$ gives

$$\sqrt{\frac{\text{var } (N'' + C'')}{\text{var } N}} = \sqrt{2C/N} \quad (56)$$

as the factor by which clutter reduces the detectability in clutter-dominated cases with optimal overresolution.

ACKNOWLEDGMENT

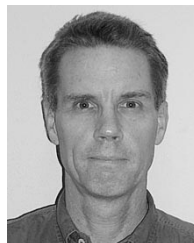
The author enjoyed fruitful discussions with M. Sulzer and would like to acknowledge P. Perillat and W. Sisk for their development of hardware and real-time software for the Arecibo long-code observations. The radar techniques sessions at the

2000 Progress in Electromagnetics Research Symposium were organized by T. Hagfors, B. Butler, T. Thompson, and G. L. Tyler, whom the author wishes to thank.

REFERENCES

- [1] G. H. Pettengill, "Measurements of lunar reflectivity using the Millstone radar," *Proc. IRE*, vol. 48, pp. 933–934, 1960.
- [2] D. O. Muhleman, B. J. Butler, A. W. Grossman, and M. A. Slade, "Radar images of Mars," *Science*, vol. 253, pp. 1508–1513, 1991.
- [3] M. A. Slade, B. J. Butler, and D. O. Muhleman, "Mercury radar imaging: Evidence for polar ice," *Science*, vol. 258, pp. 635–640, 1992.
- [4] R. N. Trebits, "Synthetic aperture radar," in *Principles of Modern Radar*, J. Eaves and E. Reedy, Eds. New York: Van Nostrand Reinhold, 1987.
- [5] D. R. Wehner, *High Resolution Radar*. Norwood, MA: Artech House, 1987.
- [6] J. C. Curlander and R. N. McDonough, *Synthetic Aperture Radar*. New York: Wiley, 1991.
- [7] N. J. S. Stacy, "High-resolution synthetic aperture radar observations of the moon," Ph.D. dissertation, Cornell Univ., Ithaca, NY, 1993.
- [8] G. H. Pettengill, S. H. Zisk, and T. W. Thompson, "The mapping of lunar radar scattering characteristics," *The Moon*, vol. 10, pp. 3–16, 1974.
- [9] R. S. Hudson and S. J. Ostro, "Shape and nonprincipal axis spin state of asteroid 4179 Toutatis," *Science*, vol. 270, pp. 84–86, 1995.
- [10] J. K. Harmon, M. P. Sulzer, P. J. Perillat, and J. F. Chandler, "Mars radar mapping: Strong backscatter from the Elysium basin and outflow channel," *Icarus*, vol. 95, pp. 153–156, 1992.
- [11] J. K. Harmon, R. E. Arvidson, E. A. Guinness, B. A. Campbell, and M. A. Slade, "Mars mapping with delay-Doppler radar," *J. Geophys. Res.*, vol. 104, pp. 14065–14090, 1999.
- [12] M. P. Sulzer, "A radar technique for high range resolution incoherent scatter autocorrelation function measurements utilizing the full average power of klystron radars," *Radio Sci.*, vol. 21, pp. 1033–1040, 1986.
- [13] —, "Recent incoherent scatter techniques," *Adv. Space Res.*, vol. 9, no. 5, pp. 153–162, 1989.
- [14] G. H. Pettengill, "Radar astronomy," in *Radar Handbook*, M. I. Skolnik, Ed. New York: McGraw-Hill, 1970.
- [15] P. E. Green, "Radar astronomy symposium report," *J. Geophys. Res.*, vol. 65, pp. 1108–1115, 1960.
- [16] R. M. Goldstein and S. Zohar, "Venus map: A detailed look at the feature β ," *Nature*, vol. 219, pp. 357–358, 1968.
- [17] D. B. Campbell and B. A. Burns, "Earth-based radar imagery of Venus," *J. Geophys. Res.*, vol. 85, pp. 8271–8281, 1980.
- [18] S. Zohar and R. M. Goldstein, "Surface features on Mercury," *Astron. J.*, vol. 79, pp. 85–91, 1974.
- [19] P. E. Clark, M. A. Leake, and R. F. Jurgens, "Goldstone radar observations of Mercury," in *Mercury*, F. Vilas, C. Chapman, and M. Matthews, Eds. Tucson, AZ: Univ. of Arizona Press, 1988.
- [20] J. K. Harmon, P. J. Perillat, and M. A. Slade, "High-resolution radar imaging of Mercury's north pole," *Icarus*, vol. 149, pp. 1–15, 2001.
- [21] G. S. Downs, P. E. Reichley, and R. R. Green, "Radar measurements of Martian topography and surface properties," *Icarus*, vol. 26, pp. 273–312, 1975.
- [22] J. K. Harmon, "A radar study of the Chryse region, Mars," *J. Geophys. Res.*, vol. 102, pp. 4081–4095, 1997.
- [23] A. F. C. Haldemann, D. L. Mitchell, R. F. Jurgens, M. A. Slade, and D. O. Muhleman, "Mars Pathfinder landing site assessment with Goldstone delay-Doppler and CW radar experiments," *J. Geophys. Res.*, vol. 102, pp. 4097–4106, 1997.
- [24] R. P. Ingalls and L. P. Rainville, "Radar measurements of Mercury: Topography and scattering characteristics at 3.8 cm," *Astron. J.*, vol. 77, pp. 185–190, 1972.
- [25] J. K. Harmon, D. B. Campbell, D. L. Bindschadler, J. W. Head, and I. I. Shapiro, "Radar altimetry of Mercury: A preliminary analysis," *J. Geophys. Res.*, vol. 91, pp. 385–401, 1986.
- [26] S. J. Ostro, J. F. Chandler, A. A. Hine, K. D. Rosema, I. I. Shapiro, and D. K. Yeomans, "Radar images of asteroid 1989 PB," *Science*, vol. 248, pp. 1523–1528, 1990.
- [27] S. J. Ostro, R. S. Hudson, R. F. Jurgens, K. D. Rosema, D. B. Campbell, D. K. Yeomans, J. F. Chandler, J. D. Giorgini, R. Winkler, R. Rose, S. D. Howard, M. A. Slade, P. Perillat, and I. I. Shapiro, "Radar images of asteroid 4179 Toutatis," *Science*, vol. 270, pp. 80–83, 1995.
- [28] S. J. Ostro, R. F. Jurgens, K. D. Rosema, R. S. Hudson, J. D. Giorgini, R. Winkler, D. K. Yeomans, D. Choate, R. Rose, M. A. Slade, S. D. Howard, D. J. Sheeres, and D. L. Mitchell, "Radar observations of asteroid 1620 Geographos," *Icarus*, vol. 121, pp. 46–66, 1996.

- [29] R. B. Dyce, G. H. Pettengill, and A. D. Sanchez, "Radar observations of Mars and Jupiter at 70 cm," *Astron. J.*, vol. 71, pp. 771–777, 1967.
- [30] S. J. Ostro, G. H. Pettengill, D. B. Campbell, and R. M. Goldstein, "Delay-Doppler radar observations of Saturn's rings," *Icarus*, vol. 49, pp. 367–381, 1982.
- [31] P. D. Nicholson, D. B. Campbell, R. G. French, G. J. Black, J.-L. Margot, and M. Nolan, "Radar images of Saturn's rings," *Bull. Amer. Astron. Soc.*, vol. 32, p. 1086, 2000.
- [32] M. S. Lehtinen and I. Häggström, "A new modulation principle for incoherent scatter measurements," *Radio Sci.*, vol. 22, pp. 625–634, 1987.
- [33] T. Hagfors and W. Kofman, "Mapping of overspread targets in radar astronomy," *Radio Sci.*, vol. 26, pp. 403–416, 1991.
- [34] —, "Correction to mapping of overspread targets in radar astronomy," *Radio Sci.*, vol. 27, pp. 231–232, 1992.
- [35] J. K. Harmon and M. A. Slade, "Radar mapping of Mercury: Full-disk images and polar anomalies," *Science*, vol. 258, pp. 640–643, 1992.
- [36] J. K. Harmon, M. A. Slade, R. A. Velez, A. Crespo, M. J. Dryer, and J. M. Johnson, "Radar imaging of Mercury's polar anomalies," *Nature*, vol. 369, pp. 213–215, 1994.
- [37] J. K. Harmon, "Mercury radar studies and lunar comparisons," *Adv. Space Res.*, vol. 19, no. 10, pp. 1487–1496, 1997.
- [38] J. K. Harmon and D. B. Campbell, "Mercury radar imaging at Arecibo in 2001," *Lunar Planet. Sci. XXXIII*, 2002, abstract 1858.
- [39] M. A. Slade, L. J. Härke, R. F. Jurgens, and H. A. Zebker, "Mercury's north and south polar regions: Goldstone radar imaging at 3.5-cm wavelength," *Bull. Amer. Astron. Soc.*, vol. 33, pp. 1026–1027, 2001.
- [40] J. K. Harmon, S. J. Ostro, J. F. Chandler, and R. S. Hudson, "Radar ranging to Ganymede and Callisto," *Astron. J.*, vol. 107, pp. 1175–1181, 1994.
- [41] L. J. Härke, H. A. Zebker, R. F. Jurgens, M. A. Slade, B. J. Butler, and J. K. Harmon, "Radar observations of the icy Galilean satellites during the 2000 opposition," *Lunar Planet. Sci. XXXII*, 2001, abstract 1369.
- [42] S. J. Ostro, R. S. Hudson, M. C. Nolan, J.-L. Margot, D. J. Scheeres, D. B. Campbell, C. Magri, J. D. Giorgini, and D. K. Yeomans, "Radar observations of asteroid 216 Kleopatra," *Science*, vol. 288, pp. 836–839, 2000.
- [43] M. C. Nolan, J.-L. Margot, and E. S. Howell *et al.*, "Arecibo radar observations of main-belt asteroids in 2000," *Bull. Amer. Astron. Soc.*, vol. 32, p. 1001, 2000.
- [44] E. O. Brigham, *The Fast Fourier Transform*. Englewood Cliffs, NJ: Prentice-Hall, 1974.
- [45] R. Bracewell, *The Fourier Transform and Its Applications*. New York: McGraw-Hill, 1965.
- [46] A. W. Rihaczek, *Principles of High-Resolution Radar*. New York: McGraw-Hill, 1969.
- [47] F. E. Nathanson, *Radar Design Principles*. New York: McGraw-Hill, 1969.
- [48] C. E. Persons, "Ambiguity function of pseudo-random sequences," *Proc. IEEE*, vol. 54, pp. 1946–1947, 1966.
- [49] M. N. Cohen, "Pulse compression in radar systems," in *Principles of Modern Radar*, J. Eaves and E. Reedy, Eds. New York: Van Nostrand Reinhold, 1987.
- [50] R. Price, "Detectors for radar astronomy," in *Radar Astronomy*, J. Evans and T. Hagfors, Eds. New York: McGraw-Hill, 1968.
- [51] J. K. Harmon, D. B. Campbell, S. J. Ostro, and M. C. Nolan, "Radar observations of comets," *Planet. Space Sci.*, vol. 47, pp. 1409–1422, 1999.



John K. Harmon was born in San Pedro, CA, in 1948. He received the B.A. degree in physics in 1970, and the M.S. and Ph.D. degrees in applied physics in 1973 and 1975, respectively, all from the University of California, San Diego (UCSD).

From 1975 to 1977, he was a Postgraduate Research Physicist at UCSD. Since 1978, he has been a member of the Planetary Radar Group, Arecibo Observatory, Arecibo, Puerto Rico, where he is currently a Senior Research Associate. Since 1992, he has also served as Assistant Director of Arecibo Observatory.

His research work has been devoted primarily to radar studies of solar system bodies, with an emphasis on terrestrial planets (Mars, Mercury) and comets. He also works on radio propagation studies of the solar wind.